High Efficiency Colloidal Quantum Dot Infrared Light Emitting Diodes via Engineering at the Supra-Nanocrystalline Level

Santanu Pradhan[1], Francesco DiStasio[1], Yu Bi[1], Shuchi Gupta[1], Sotirios Christodoulou[1], Alexandros Stavrinadis[1] and Gerasimos Konstantatos[1, 2]*

[1]ICFO-Institut de Ciencies Fotoniques, The Barcelona Institute of Science and Technology, 08860 Castelldefels (Barcelona), Spain

[2]ICREA—Institució Catalana de Recerca i Estudis Avançats, Passeig Lluís Companys 23, 08010 Barcelona, Spain

* gerasimos.konstantatos@icfo.es

Colloidal Quantum Dot (CQD) light emitting diodes (LEDs) have delivered compelling performance in the visible, yet infrared CQD LEDs underperform their visible-emitting counterparts, largely due to their low photoluminescence quantum efficiency (PLQE). Herein, we employ a ternary blend of CQD thin film comprising a binary host matrix that serves to electronically passivate as well as to cater for efficient and balanced carrier supply to the emitting QD species. In doing so, we report on infrared PbS CQD LEDs with external quantum efficiency of ~7.9% and power conversion efficiency of ~9.3%, thanks to their very low trap-state density on the order of 10^{14} cm^{-3} and very high PLQE in electrically conductive QD solids of more than 60%. When these blend devices operate as solar cells they deliver V_{OC} approaching their radiative limit thanks to the synergistic effect of reduced trap state density and the density of states modification in the nanocomposite.

Near and short-wave infrared (NIR, SWIR) light emitting diodes serve a rather broad range of applications, including night vision[1], surveillance[2], remote sensing[3], biological imaging[4] and spectroscopy[5]. Recent progress in on-chip and wearable infrared spectroscopy for quality inspection, health and process monitoring also requires the development of highly efficient,

CMOS-compatible and low cost NIR and SWIR LEDs[6,7,8]. In contrast to other highly performant solution processed materials such as polymers and dyes, whose bandgaps are mainly limited in the visible, CQDs offer a unique opportunity as they readily provide access to both the visible[9,10,11,12] and the infrared parts of spectrum[13]. In view of this, several efforts employing core-shell structures[14,15], inter dot spacing engineering[16,17], chemical passivation with perovskite[18] and organic-inorganic hybrid[19] approaches have been made to develop efficient CQD infrared-emitting LEDs. The use of core-shell CQD structures[14,15] to increase the PLQE, have reached EQE in excess of 4%. Alternatively, the use of appropriate host matrices has been considered as a means to suppress PLQE quenching in close-packed CQDs due to energy transfer. Initial reports have employed polymer host matrices[20,21,22,23], yet with limited EQEs mainly due to the polymers' poor electron transport properties. Recently, an alternative matrix has been reported based on perovskite materials epitaxially connected to the CQD emitting species serving both as a chemical passivant of the QD surface and as an efficient carrier transport matrix, leading to EQE of 5.2% and power conversion efficiency (PCE) of 4.9%[18]. PCE in LEDs is defined as the ratio of optical output power over the electrical input power and it is of paramount importance when considering the power consumption of the device.

We posited that instead of relying solely on chemical passivation of the CQD emitting species, the use of a remote charge passivation mechanism induced from an appropriate matrix would be more robust and efficient in reducing trap state density in the CQDs[24,25]. Unlike prior approaches[18,22], our implementation is based entirely on CQD materials. In doing so, we exploited the advances made in QD solids in terms of mobility and carrier diffusion length thanks to the progress in photovoltaic devices[26,27,28], in which mobilities and carrier diffusion lengths in excess of $\sim 10^{-2}$ cm^2 V^{-1} s^{-1} and 230 nm respectively, have been reported , fulfilling the needs for efficient carrier transport in the typical thinner-than-solar-cells, LED devices.

LED Architecture and Performance

We have considered two LED architectures, one comprising a binary blend of small PbS QDs with large bandgap serving as the carrier supplier for the large PbS QDs with smaller-bandgap that act as the carrier acceptor and emitting species (Fig. 1a). The second case comprises a ternary blend formed by the binary blend with the addition of ZnO nanocrystals (NCs), which serve as a high-bandgap electron-rich transporting medium and that is employed to further balance carrier injection in the active region as well as to further passivate remotely the traps of the PbS QDs[24] (Fig. 1b). The ligand exchange scheme that was employed for the active layers was based on a mixture of zinc iodide and 3-mercapto-propionic-acid (MPA) as it has delivered previously solar cells with long carrier diffusion lengths and high open circuit voltage[29] (see Methods for the details of device fabrication). Both structures also employ a ZnO front layer as an electron injecting, hole-blocking layer and 1, 2-Ethanedithiol (EDT) treated small PbS QD layer on top that facilitates hole injection and electron blocking at the back interface. The thickness of each of the layers used in high performance devices considered in this study are illustrated in the cross-sectional focused ion beam SEM images in Fig. 1c,d for the binary and ternary blends respectively. Typically, the optimal thickness of electron injecting, active and hole injecting layers are around 80 nm, 60 nm and 70 nm respectively. The TEM images of Fig. 1 illustrate the effective blending of these QD species at the nanoscale and support the nature of the nanocomposite active layer. The corresponding band diagrams of the constituent materials used in these devices are shown in Fig. 1e, taken from UV photoelectron spectroscopy measurements[28,30] (UPS). According to this, both ZnO NCs and small PbS QDs serve as a type-I heterostructure with the emitting large PbS QDs. The small PbS QD matrix forms a marginal type-I heterostructure with the large PbS QD emitters in which the band offset confinement for both electrons and holes is between 0.1-0.2 eV. Based on the band diagram electron transport and injection takes place within the ZnO NC and the

small PbS QD matrix given their matched conduction band levels, whereas hole transport is facilitated largely via the small PbS QD matrix.

Figure 2a shows the radiance of the binary and ternary blend-based LED devices with applied bias voltage. The control device comprising only large PbS QD as the active layer is also plotted for comparison. All devices showed very high radiance of ~9 W sr^{-1} m^{-2} at 3.5 V, which is more than 50% higher compare to the previously reported PbS QD based IR LEDs [16,18]. It is noteworthy that the turn-on voltage for both binary and ternary blend devices is around 0.6 V, i.e. below the bandgap of emission, while the turn-on voltage of the control device was 0.87 V, i.e. matching closely the bandgap of emission (note: we have considered 1 nW radiance as the turn on power). The electroluminescence spectra with different values of voltage bias for the ternary device are shown in Fig. 2b with clear band-edge electroluminescence emission at sub-band gap voltages. This is the lowest turn-on voltage ever reported for a PbS QD based LED. Although this below-bandgap turn-on value is not thermodynamically feasible in the absence of multi-carrier processes, it has been reported previously for polymer[31] and QD based LEDs[11], attributed to Auger assisted charge injection processes. According to this, the low-energy barrier for electron injection results in electron accumulation at the active layer and hole transporting layer (HTL) interface which can fulfil the condition for Auger assisted charge injection[11,31,32,33]. In our case, we attribute this partially to the improvement of mobility and trap passivation with the mixed ligand treatment employed herein as well as the use of bulk heterojunctions. To examine the hypothesis about the role of the ligand passivation we fabricated a ternary blend active layer device using only MPA as the ligand (MPA ligand exchange yields carrier mobility lower than the ZnI$_2$_MPA treatment). The device showed a much higher turn-on voltage (2.5 V) and lower radiance compared to the devices reported in this manuscript (Fig. S2). An additional plausible mechanism can be assigned to Auger assisted recombination in the small PbS QD matrix in which hole transport takes place via midgap

delocalized states[34,35] and recombination with electrons transfers the energy to the remaining holes in those states enabling them to move to the valence band and subsequently inject into the emitting QDs. Yet, we consider that further studies are needed to shed light into this interesting effect.

Despite the similar radiance measured across those three LED devices, a large difference in their driving currents was recorded, with the control (single) device yielding very high leakage current that progressively decreases in the binary and ternary blend cases as shown in Fig. 2c. This has a significant effect in the EQE of the LEDs as shown in Fig. 2d. The peak EQE of the ternary device reached 7.87 % (average: (7.11 ± 0.30) %, Fig. S3) compared to 0.38 % ((0.3±0.07) %) for the single and 4.5% ((4.12±0.29) %) for binary QD based devices. The ternary blend based devices have reached record high EQE for CQD LEDs emitting at 1400 nm wavelength. Previously reported best devices showed the peak EQE around 5% covering a similar spectral range[14,15,18]. We attribute this to the trap passivation and the reduction of leakage current in the blend-devices. The high EQE recorded in the binary and ternary blend devices, taken together with the low turn-on voltage results also in unprecedentedly high PCE. Figure 2e plots the PCE of the LED devices from which the ternary blend based device outperforms with a peak PCE as high as 9.3%, a nearly twofold improvement over the previous record[18]. The synergistic use of both PbS QD matrix dots and ZnO NCs has been instrumental in reaching high EQE. Binary control devices comprising PbS QD emitters with ZnO NCs have reached an optimum EQE of 1.8% (Fig. S4).

In course of device optimization and in order to demonstrate the versatility of this approach, we have fabricated and measured ternary devices with optimized blend ratio varying the bandgap of the PbS QD matrix as well as the bandgap of the PbS QD emitters, the results of which are summarized in Table 1. The electroluminescence spectra of various emitting PbS QD bandgaps are shown in Fig. S5a. The variation of the PbS QD matrix bandgap (Table 1 and

Fig. S5b) revealed that optimized EQEs are achieved with increasing the bandgap of the PbS QD matrix, likely due to more efficient charge transfer to the emitting PbS QDs and increased confinement in the emitting QDs due to the larger band offset with the surrounding PbS QD matrix. Considering the fact that our devices are based entirely on CQD components with reported high stability[28,36], we have tested the stability of the best performing device under a constant applied current over a period of 48 hours. The radiance and the EQE of the device are highly stable throughout the course of the test as shown in Fig. 2f, especially considering that the devices were fabricated and characterised in ambient air conditions without any encapsulation.

Photoluminescence Quantum Efficiency Studies

The origin of this high EQE lies on very high PLQE of the QD films employed and we therefore explored in more depth the role of the host matrix on the PLQE of the emitting QD species. In Figure 3a, we plot the PL spectra for the ligand exchanged binary blend films varying the loading of emitting QDs in the small PbS QD matrix. We firstly note that the position of the PL peak of the emitter QDs does not alter with varying concentration suggesting the absence of exciton transfer amongst them, consistent with the Förster radius value of 3.5 nm for the energy transfer among the emitter QDs and their much larger inter-dot spacing in the blends (see Supplementary information S6). The absence of PL emission from the matrix QDs upon blending corroborates the highly efficient carrier transfer from the matrix QDs to the emitting QDs and suggests that energy transfer between those species is not present considering the small Forster radius of 1.6 nm for the matrix – emitter QD system (see Supplementary information S6). This finding is in accordance to prior reports in which such high charge transfer has been ascribed to the increased coupling strength enabled in ligand exchanged electronically coupled QD solids[37]. Here, we have made use of this effect to develop QD solids with considerably high PLQE under the following rationale: For a given density of poorly

emitting (defective) large PbS QDs and a given QD film volume we envision a much higher PLQE when the large PbS QDs are introduced into a small PbS QD matrix, due to the proportionally lower number of defective large PbS QDs existent in the same volume. This hypothesis is valid when the matrix is absorbing at the optical excitation wavelength and possess long carrier diffusion lengths to supply the emitting QD species with electrons and holes. The schematic representation of this mechanism is illustrated in Fig. 3d,e. PLQE measurements of such binary blends are in agreement with the proposed mechanism. Fig. 3b plots the PLQE values of the binary blends varying the emitter QD loading in the host PbS QD matrix. An optimum PLQE of 60% is recorded for a loading of 10% of emitter PbS QDs in a donor PbS QD host matrix, drastically increased over the 2.3% PLQE of the neat emitter PbS QD film. This is a remarkably high PLQE considering that refers to electronically conductive ligand exchanged QD solids. Such high PLQE values for the binary case should also express in long PL lifetimes. The transient PL of the 7.5% loaded binary blend, shown in Fig. 3c, yields a bi-exponential decay with corresponding lifetimes of 632 ns and 2.99 μs (fitting values are summarised in Supplementary information S7). The first decay is attributed to the intrinsic PL lifetime of the emitter QDs whereas the longer component is associated to the carrier supply time of photo-generated carriers in the matrix of the binary blend to diffuse and excite the emitter QDs. The shorter component of 632 ns is in agreement with the recorded PLQE values considering that the ideal radiative lifetime of PbS has been reported on the order of 1 μs[38,39]. Increasing the amount of emitter QDs in the matrix reduces the PLQE as a result of increasing the probability of non-radiative recombination in the defective emitter QDs. Whereas decreasing the amount of emitter QDs in the matrix reduces the PLQE as a result of increasing the probability of non-radiative recombination in the host matrix considering a carrier diffusion length around 70 nm in the small PbS QD matrix[37]. Although the 10% emitter QD based binary

blend yields the best PLQE, it does not yield the best EQE among different binary blends (Fig. S10). We attribute this to the trade-off between efficient balanced charge injection and PLQE.

The synergistic use of ZnO NCs, in addition to improving balance of charge injection (as shown in Fig. 2c), offers the additional benefit of remotely passivating electron traps in the PbS QD emitters. The electrons of the n-type ZnO NCs, when in the vicinity of PbS QDs with electron traps available for population are used to electrically passivate those electron traps and result in higher radiative recombination efficiencies[24,25] (Fig. 3f). The PLQE of the ternary blend films as a function of PbS QD emitter loading in the PbS QD host matrix at a given ZnO loading of 40% is presented in Fig. 3b. According to this, a further increase in PLQE approaching a value of 80% for a loading of 20% of the emitting QD species is observed. The PLQE of the ternary blends with different PbS QD and ZnO ratios are shown in Fig. S11. In all types of PbS QD combinations, 40% ZnO loading in ternary blend gives the best PLQE and also the best EQE in LED devices, as shown in Fig. S12. It is noteworthy that the loading of emitter QDs in donor matrix or addition of ZnO NCs does not cause any spectral shift in the PL (Fig. S13), suggesting thus that the observed increase in the PLQE of the emitting PbS QDs is not due to suppression of energy transfer amongst them. Similar to the binary case, transient PL measurement of the ternary system exhibits a bi-exponential PL lifetime with the first component, associated to the radiative lifetime, on the order of 827 ns and the second one longer lived, associated to the carrier diffusion from the matrix PbS QDs to the emitter QDs, on the order of 3 μs.

These high PLQE values are also in line with the quantum efficiency values reported in the LED devices. In Fig. S14, we plot the internal quantum efficiency (IQE) of the LED devices defined as the ratio of photon generated inside the device to the injected charge carriers. The ternary blend devices yield a peak IQE value of 33.3% whereas the binary blend shows IQE of 17.5%. The improvement in EQE and thereby IQE is nearly twofold, i.e. much higher than the

improvement in the PLQE. In Table 2 we summarize the different efficiency factors that determine the EQE of an LED according to the following equation[18]:

$$IQE = PLQE \times \eta_{carrier\ supply} \tag{1}$$

Where carrier supply efficiency ($\eta_{carrier\ supply}$) measures how efficiently balanced carrier injection takes place and transported at the active layer of the LED. IQE is estimated as per Fig. S14 using the experimentally determined EQE and the optical loss model. The experimentally determined values of IQE and PLQE allow us to estimate the $\eta_{carrier\ supply}$ of the three classes of devices. While the single LED yields the highest carrier supply efficiency its performance is limited by the low PLQE of the active layer. The binary LED improves on the PLQE factor yet suffers from low carrier supply to the emitter QDs. The ternary system yields a more efficient carrier supply over the binary along with higher PLQE leading to an overall higher EQE. This shows that our current LED devices are carrier supply limited and further improvement in EQE can be within reach through device optimization. It also supports the hypothesis that the use of ZnO serves a twofold role: it improves the trap passivation and PLQE, as well as improves the balance of carrier injection at the optimal LED configuration (40% ZnO loading).

Performance of blend devices as solar cells

A highly performing LED material, i.e. one having very high PLQE, is expected to be the ideal material for solar cell applications in demonstrating open circuit voltage (V_{OC}) very close to the radiative limit[40,41,42]. Having recorded such high PLQE values in electrically conductive QD solids in the present work, led us to test this expectation herein. We have therefore constructed photovoltaic (PV) cells based on the architectures considered previously for the LED devices, essentially mimicking the LED structures with instead much thicker active layer to facilitate high optical absorption. The thickness of electron transporting, active and hole

9

transporting layers were around 40 nm, 220 nm and 30 nm respectively and the PV structure followed a typical CQD solar cell[43]. The dark J-V characteristics, plotted in Fig. 4a, provide initial features of suppressed recombination upon blending, as evidenced by the significantly lower reverse current of the blended-layer diodes compared to the single QD-layer diode case. The J-V curves of those cells under simulated AM1.5 solar illumination is shown in Fig. 4b. The V_{OC} of the binary device increased to 0.59 V from 0.39 V of the single QD based device, which is a typical V_{OC} value for PbS QD solar cells of the same bandgap[28]. The large V_{OC} deficit (defined as the deficit of V_{OC} from the bandgap voltage) for PbS QD based solar cells has been believed to be a result of significant presence of non-radiative, in-gap traps[44]. The increased V_{OC} (and subsequent decrease in V_{OC} deficit) can therefore stem from reduced trap state density in accordance to the drastically improved PLQE values recorded for the binary blend films (Fig. 3b). The addition of ZnO further improves V_{OC} to a value of 0.69 V for the ternary blend device. This is a notably large value of V_{OC} that approaches the radiative limit[40] considering the fact that the solar cell harnesses photons with energies down to 0.92 eV. We have calculated the radiative V_{OC} limit of the PV devices following standard analysis (Supplementary information S13)[40,41]. Figure 4c summarises the radiative limit and non-radiative loss of the V_{OC}. Non-radiative losses decrease with binary blending compared to the single QDs and further decrease in ternary blend devices with ZnO loading. The EQE spectra of these solar cell devices (Fig. 4d) demonstrate their spectral reach down to 1400 nm, determined by the low-bandgap PbS QDs. Naturally the EQE in the infrared is reduced in the case of binary blend due to the low loading of the large PbS QDs in the blend and its consequent lower absorption. In the case of ternary we observe a more drastic reduction in EQE across the spectrum which is ascribed to the poor electron transport through the ZnO NC network[24,25].

Theoretically, Gong *et al.* have shown the influence of trap-state reduction on the enhancement of radiative recombination[18]. To further characterize and quantify the degree of trap-state

passivation upon blending, we have employed thermal admittance spectroscopy (TAS). TAS allows us to obtain a quantitative picture of the in-gap trap distribution of the photoactive material as previously demonstrated on different types of PV devices[45,46]. The detailed analysis of the employed method is described in the Supplementary information S14. The trap distribution as a function of E_t (position of trap state with respect to the band-edge) deduced from TAS analysis gives a clearer picture of trap reduction upon QD blending as shown in Fig. 4e. E_t decreases only slightly from 0.254 eV for single QD based device to 0.237 eV for binary blending yet it is further reduced to 0.174 eV for ternary blends. The position of E_t follows similar trend like trap activation energy (E_A) as determined from Arrhenius plot (Fig. S18). The overall trap-state density decreased from 10^{16} cm^{-3} for single QDs based device to 4.8×10^{15} cm^{-3} for binary QDs and further down to 6.5×10^{14} cm^{-3} for ternary QDs based device. These results from TAS also corroborate our hypothesis on the passivation mechanism at play upon binary and ternary blending. In case of binary blending there is an overall effective reduction of trap states without much alteration of the energetic value of the traps, i.e. their nature; this is in accordance to the model described in Fig. 3e. Upon ternary blending, in addition to the reduction of the trap density, there is also a significant lowering of the trap-state depth due to the remote passivation facilitated by the ZnO NCs (Fig. 3f). It must be noted that TAS technique measures the overall trap state density of the blend and cannot distinguish between traps in the emitter QDs and the matrix QDs. However, in case of the ternary blend the resultant trap state density per emitter QD is one order of magnitude lower than that of single providing strong evidence of the trap state reduction upon the use of ZnO NCs (Supplementary information S15).

In order to thoroughly examine whether the trap state reduction is the sole responsible for this notable increase in V_{OC}, we performed SCAPS simulations of a single layer device in which we have varied the trap state density across the experimentally obtained range of values.

According to SCAPS the expected V_{OC} increase from single to binary to ternary devices is 40 mV and 100 mV respectively, whereas the observed increase in V_{OC} from single to binary is around 200 mV. SCAPS simulations confirm that upon trap state reduction from single to binary V_{OC} increases but to a lesser extent than what we have experimentally measured, whereas the further increase in V_{OC} from binary to ternary is accounted for trap state reduction. We therefore sought additional mechanisms at play in the binary blends that may contribute to this high value of Voc. The binary blend devices comprise ~7.5% lower bandgap emitter QDs embedded in a larger bandgap matrix QDs. Therefore, the density of states (DOS) of the low bandgap QDs in a binary device is reduced over the DOS of the single layer counterpart. In Supplementary information S16, we present a more detailed model which takes into account the effective reduction of the DOS of the binary blend. This reduction of the DOS yields an improvement in V_{OC} ~120 mV when only the emitter QDs are excited and ~160 mV upon excitation of both the matrix and emitter QDs. During the revision of this manuscript Sun *et al.* have also reported the effect of DOS reduction on the V_{OC} of CQD blended solar cells, yet in a different bandgap mixing regime[47]. To further corroborate this hypothesis, we plot in Fig. 4f the intensity and wavelength dependence of the V_{OC} for the three classes of devices. In agreement with SCAPS modelling (Fig. S22), the V_{OC} of the single device is independent of the photon energy for the same intensity whereas in the case of blend devices lower energy photons of 1310 nm (that excite only the low bandgap QDs) yield lower V_{OC} than higher energy photons of 637 nm (that excite both the low bandgap and matrix QDs). These measurements support our hypothesis of combined effect of trap state reduction and DOS modification on the V_{OC} improvement with blend structures compared to the emitter only devices.

Conclusion

In summary, we report a new approach of engineering quantum dot solids at the supra-nanocrystalline level that has led to record low trap state density, very high PLQE values in

solid-state conductive QD films and thereby highly efficient LEDs. The use of different bandgap QDs also offers a leverage to tune the density of states in quantum confined nanocomposite solids that has allowed us to reach very high open circuit voltage when these devices have been operated as solar cells. This work offers new insights in engineering the energetic potential landscape of QD solids with important implications towards higher performance light emitters and solar cells.

Author contributions

G.K. proposed the idea and directed the study. S.P. co-developed the concept, fabricated, characterized the devices and analyzed the data. S.P. and G.K. designed the experiments with the help of F.D.S. F.D.S. performed the PLQE and EL studies and processed the results. Y.B. and S.G. synthesized the materials. S.C. performed TEM imaging. A.S. performed SEM imaging. G.K. and S.P. wrote the manuscript with inputs from coauthors.

Additional information

Supplementary information is available in the online version of the paper. Reprints and permissions information is available online at www.nature.com/reprints.

Correspondence and request for materials should be addressed to G.K.

Competing financial interests

G.K and S.P have filed a patent application related to this work.

Methods

Synthesis of PbS QDs:

Schlenk technique was used to synthesize PbS QDs. 830 nm and 940 nm excitonic peak based PbS QDs were synthesized following the standard recipe. 2 mmol lead oxide (PbO), 4.7 mmol oleic acid, and 9.4 mmol 1-octadecene (ODE) were pumped overnight at 95 $^{\circ}$C. Then 15 mL of ODE was added and the temperature of the reaction was adjusted to 75 $^{\circ}$C or 100 $^{\circ}$C for 830 nm and 940 nm PbS QDs, respectively. When the temperature point is reached, 1 mmol hexamethyldisilane (TMS) mixed with 10 mL ODE was immediately injected. The heating was stopped (without removing the heating mantle) and the sample allowed to cool down gradually (~1 h). The NCs were isolated by adding acetone and then centrifuged, purified by dispersion/precipitation with toluene/acetone 3 times, and finally dispersed in anhydrous toluene (30 mg mL^{-1}) before using them for device formation.

1300 nm excitonic peak based PbS QDs were synthesized by a previously reported multi-injection method with modifications[48]. Typically, PbO (0.45 g), oleic acid (3.8 mL) and ODE (50 mL) were mixed together at 95 $^{\circ}$C under vacuum for 12 h. Then the temperature of the reaction was raised to 100 $^{\circ}$C. The solution of 90 μL TMS in 3ml ODE was injected, the additional 3 injections (25 μL TMS in 3 mL ODE for each injection) were sequentially followed by a fixed time. When the injection was finished, the heating was stopped immediately and the sample was allowed to cool down gradually to room temperature under constant stirring. QDs were precipitated by adding acetone, followed by centrifugation, purified in air by using toluene/acetone as solvent/anti-solvent. The final QDs were dispersed in toluene with a concentration of 30 mg mL^{-1} for device fabrication.

ZnO nanocrystals preparation:

ZnO nanocrystals were prepared following a previously reported method[24]. 2.95 g zinc acetate dihydrate was dissolved in 125 mL methanol under vigorous stirring and the temperature of

the solution was set at 60 °C. At the same time, in a separate vial 1.48 g KOH (90%) was dissolved in 65 mL methanol solution. The prepared KOH solution was then added dropwise to the zinc acetate solution for a period of 4 minutes while the temperature was kept at 60 °C with constant stirring. The reaction conditions were left unaltered for the next 2.5 hours. After completion of the reaction, the heating source was removed and the solution was allowed to cool down slowly to room temperature. The solution was then centrifuged at 3500 rpm for 5 min. The supernatant was discarded and an equal amount of methanol was added and centrifugation repeated. After three rounds of purification, the NCs were dispersed in a solution of 2% butylamine in chloroform for base layer formation and in 5% butylamine in toluene for ternary blend formation.

LED device preparation:

LEDs were prepared on cleaned ITO coated glass. The electron transporting layer (ZnO) was prepared by spin coating ZnO nanocrystals in chloroform (40 mg mL^{-1}) with a spin speed of 4000 rpm. The procedure was repeated once more to have a thicker film of approximately 80 nm. The active emitting layer was grown on top of the ZnO layer. Before mixing, all QDs and ZnO NC solutions were prepared in separate vials with the same concentration (30 mg ml^{-1}). For binary blends, emitter PbS QDs were mixed to donor PbS QDs with different volume ratios. Ternary blends were formed by mixing ZnO NC solution to the binary blend with different volume ratios. During the film formation, QDs were treated with ZnI_2 and MPA mixed ligand as described in our previous report[29S]. The mix ligand was prepared by mixing 25 mM ZnI_2 in methanol and 0.015% MPA in methanol solutions. The ZnO substrates were covered with 50 µL of QD solutions and spun immediately with 2500 rpm for 15 sec. Then, the spin coater was stopped to add few drops of mixed ligand to treat for 5 sec. After that, the spincoater was started to dry the film which was then washed with few drops of methanol. The procedure was repeated thrice to get an average thickness of 60 nm. The hole transporting layer was formed by using small diameter PbS QDs treated with 0.02% EDT in acetonitrile solution. The back electrode was formed with Au deposition through a pre-patterned shadow mask in thermal evaporator (Nano 36 Kurt J. Lesker) at a base pressure of 10^{-6} mbar. The active area for each device is 3.14 mm^2.

LED performance characterization:

 All the devices were fabricated and characterized in ambient air conditions. Current density–voltage (J-V) characteristics were recorded using a computer-controlled Keithley 2400 source

measurement unit. To calculate the EQEs, electroluminescence from the front face of the device was detected using a calibrated Newport 918D-IR-OD3 germanium photodetector connected to Newport 1918-C power meter in parallel to the J–V measurements. A Shadow mask of 3 mm in diameter was placed in front of the device to minimize the waveguide effect from ITO coated glass. Lambertian emission was assumed. The thickness of the glass substrate was considered during the solid angle measurement. The radiance was further verified with a NIST certified 818-IG InGaAs photodetector with calibrated DB15 module by Newport.

PL, PLQE & PL decay measurements:

PL measurements were performed using a Horiba Jobin Yvon iHR550 Fluorolog system coupled with a Hamamatsu RS5509-73 liquid-nitrogen cooled photomultiplier tube, and a calibrated Spectralon™ coated Quanta-phi integrating sphere. All reported steady-state PL spectra and photoluminescence quantum efficiency (PLQE) measurements were collected using a continuous-wave Vortran Stradus 637 laser diode as excitation source (λ = 637 nm, maximum power = 80 mW), and all reported steady-state PL spectra have been corrected for the system response function. Both binary and ternary blend films used in the PL measurements were prepared via aforementioned layer-by-layer deposition using the mixed-ligand-exchange procedure (5 layers) onto (3-mercaptopropyl) trimethoxysilane (MPTS) functionalized glass. Such treatment was used to improve the adhesion of the QDs on glass to obtain continuous and uniform QD films. The treatment was performed prior QDs deposition by inserting 1x1cm glass substrates into a petri dish containing a MPTS toluene solution (10% by volume) then removed after 24h and gently dried under a flux of nitrogen.

The PLQE measurements were carried out as following: initially, the PLQE of a 100 nm thick film of PbS QDs (reference film) was measured inside the calibrated integrating sphere using the procedure proposed by De Mello et al.[49] (λ_{PL} =1125 nm, film was fabricated following the method described above) (Supplementary information S17) yielding a PLQE of 24 ± 3%. The emission intensity of the film was then measured in the sample chamber of the fluorimeter (i.e. outside the integrating sphere) using predetermined and fixed excitation and collection conditions. By comparing the emission intensity measured outside and inside the integrating sphere, and the optical absorption at the excitation wavelength obtained inside the integrating sphere, we obtained a correction factor (i.e. the PLQE of the reference film calculated using the number of emitted photons measured in the fluorimeter sample chamber and the number of absorbed photons measured in the integrating sphere was 48 times higher than the real value). Afterward, all other films were measured using the same procedure (number of absorbed

photons measured inside the sphere, number of emitted photons measured in the fluorimeter sample chamber) using the predetermined and fixed excitation and collection conditions employed for the reference film, and the correction factor was applied to obtain the PLQE value.

The above method was employed for all the PLQE values reported in the manuscript as it was not possible to use the Quanta-phi integrating sphere for $\lambda_{PL} > 1200$ nm as the fibre bundles interfacing the Quanta-phi integrating sphere to the Horiba Jobin Yvon iHR550 Fluorolog system are not transparent in this spectral range. The obtained correction factor from the reference film accounts for the response function of the whole fluorimeter and detector. Yet, considering the different emission wavelength of the reference film ($\lambda_{PL} =1100$ nm) and the blended films ($\lambda_{PL} =1371$ nm), a deviation of the correction factor value can arise from the different spectral reflectivity of the sphere although Spectralon™ presents small reflectance variation in this spectral region (less than 1%). The PL decay measurements were performed using Horiba spectraLED - S-625 excitation source ($\lambda = 637$ nm) with time resolution of 300 ns.

EL measurements:

Spectral EL measurements were also performed using a Horiba Jobin Yvon iHR550 Fluorolog system coupled with a Hamamatsu RS5509-73 liquid-nitrogen cooled photomultiplier tube. The voltage bias to the device was applied with a Keithley 2400 source measurement unit. The acquired spectra were corrected using the system response factor provided by the manufacturer.

Photovoltaic device preparation and characterizations:

The PV device preparation follows a similar procedure as the LED described above other than the thickness of the respective layers. The ZnO base layer was deposited thinner compared to LED device (~40 nm). The active layer was prepared much thicker in order to absorb sufficient photons (~200-220 nm). Finally, 2 layers of EDT treated PbS (~30-35 nm) were used as electron blocking layer. Approximately 100 nm Au was deposited as the back electrode. The active area of the device was 3.14 mm^2. All the PV characterizations were performed in ambient conditions. The device I-V responses were collected using a Keithley 2400 source meter. Illumination intensity of AM 1.5 was maintained using a class AAA solar simulator (Oriel sol3A, Newport Corporation). The accuracy of the measurement was determined as ±4%. EQE measurements were performed with an in-house built experimental set-up by using chopped (220 Hz, Thorlab) monochromatic illumination. The power was measured with a

calibrated Newport-UV power meter. The device response of the chopped signal was measured using a Stanford Research system lock-in amplifier (SR830) which was fed by a Stanford Research system low noise current pre-amplifier (SR570). The final EQE spectra were obtained with the help of LabVIEW program. The intensity dependent V_{OC} measurements were performed with Vortran (637 nm) and Superk Extreme (NKT photonics, 1310 nm) lasers.

Thermal admittance spectroscopy (TAS) measurements:

The measurements were performed with the PV devices in a Lakeshore four probe cryogenic chamber controlled by a Lakeshore-360 temperature controller. The frequency dependent capacitance was measured with an Agilent B1500 connected with an external capacitance measurement unit. The temperature was varied from 220 K to 320 K to acquire the frequency dependent capacitance variation. The voltage dependent capacitance was measured with the same instrument in order to obtain the value of depletion width and built-in voltage. The detailed data analysis procedure is described in the Supplementary information S11.

TEM measurements:

The bright field (BF) TEM images of the films have been obtained with JEOL JEM-2100 (LaB_6 electron gun) transmission electron microscope, operating at 200 kV. The samples were prepared by spin coating the QD solutions onto 300-mesh carbon-coated copper grid at 2500 rpm. Then, the ligand exchange with ZnI_2_MPA was performed in line with the aforementioned device fabrication procedure.

Data Availability

The data that support the plots within this paper and other findings of this study are available from the corresponding author upon reasonable request

References:

(1) Borek, C. *et al.* Highly efficient, near-infrared electro phosphorescence from a Pt-metalloporphyrin complex. *Angew. Chem.* **46,** 1109–1112 (2007).

(2) Goossens, S. *et al.* Broadband image sensor array based on graphene–CMOS integration. *Nat. Photonics* **11,** 366–371 (2017).

(3) Murphy, C. J. Optical sensing with quantum dots. *Anal. Chem.* **74,** 520A–526A

(2002).

(4) Medintz, I. L., Uyeda, H. T., Goldman, E. R. & Mattoussi, H. Quantum dot bio conjugates for imaging, labelling and sensing. *Nat. Mater.* **4,** 435–446 (2005).

(5) Voura, E. B., Jaiswal, J. K., Mattoussi, H. & Simon, S. M. Tracking early metastatic progression with quantum dots and emission scanning microscopy. *Nat. Med.* **10,** 993–998 (2004).

(6) Park, S. I. *et al.* Soft, stretchable, fully implantable miniaturized optoelectronic systems for wireless optogenetics. *Nat. Biotechnol.* **33,** 1280–1286 (2015).

(7) Kim, J. *et al.* Battery-free, stretchable optoelectronic systems for wireless optical characterization of the skin. *Sci. Adv.* **2,** e1600418 (2016).

(8) Lopez,́ A., Arazuri, S., García, I., Mangado, J. & Jaren, C. A review of the application of near-infrared spectroscopy for the analysis of potatoes. *J. Agric. Food Chem.* **61,** 5413−5424 (2013).

(9) Shirasaki, Y., Supran, G. J., Bawendi, M. G. & Bulović, V. Emergence of colloidal quantum-dot light-emitting technologies. *Nat. Photonics* **7,** 13–23 (2013).

(10) Pal, B. N. *et al.* 'Giant' CdSe/CdS core/shell nanocrystal quantum dots as efficient electroluminescent materials: strong influence of shell thickness on light-emitting diode performance. *Nano Lett.* **12,** 331-336 (2012).

(11) Mashford, B. S. *et al.* High-efficiency quantum-dot light-emitting devices with enhanced charge injection. *Nat. Photonics* **7,** 407–412 (2013).

(12) Dai, X. *et al.* Solution-processed, high-performance light-emitting diodes based on quantum dots. *Nature* **515,** 96–99 (2014).

(13) Hines, M. A. & Scholes, G. D. Colloidal PbS nanocrystals with size-tunable near-infrared emission: observation of post-synthesis self-narrowing of the particle size distribution. *Adv. Mater.* **15,** 1844-1849 (2003).

 (14) Supran, G. J. *et al.* High-performance shortwave-infrared light-emitting devices using core–shell (PbS–CdS) colloidal quantum dots. *Adv. Mater.* **27,** 1437–1442 (2015).

(15) Yang, X. *et al.* Iodide capped PbS/CdS core-shell quantum dots for efcient long wavelength near-infrared lightemitting diodes. *Sci. Reports* **7,** 14741 (2017).

(16) Sun, L. *et al.* Bright infrared quantum-dot light-emitting diodes through inter-dot spacing control. *Nat. Nanotechnol.* **7,** 369–373 (2012).

(17) Yang, Z. *et al.* All-quantum-dot infrared light-emitting diodes. *ACS Nano* **9,** 12327–12333 (2015).

(18) Gong, X. *et al.* Highly efficient quantum dot near-infrared light-emitting diodes. *Nat. Photonics* **10,** 253–257 (2016).

(19) Bourdakos, K. N., Dissanayake, D. M. N. M., Lutz, T., Silva, S. R. P. & Curry, R. J. Highly efficient near-infrared hybrid organic-inorganic nanocrystal electroluminescence device. *Appl. Phys. Lett.* **92,** 153311 (2008).

(20) Colvin, V. L., Schlamp, M. C. & Alivisatos, A. P. Light-emitting diodes made from cadmium selenide nanocrystals and a semiconducting polymer. *Nature* **370,** 354–357 (1994).

(21) Tessler, N., Medvedev, V., Kazes, M., Kan, S. & Banin, U. Efficient near-infrared polymer nanocrystal light-emitting diodes. *Science* **295,** 1506-1508 (2002).

(22) Konstantatos, G., Huang, C., Levina, L., Lu, Z. & Sargent, E. H. Efficient infrared electroluminescent devices using solution-processed colloidal quantum dots. *Adv. Func. Mater.* **15,** 1865–1869 (2005).

(23) Roy Choudhury, K., Song, D. W. & So, F. Efficient solution-processed hybrid polymer–nanocrystal near infrared light-emitting devices. *Org. Electron.* **11,** 23-28 (2010).

(24) Rath, A. K. *et al.* Remote trap passivation in colloidal quantum dot bulk nano-heterojunctions and its effect in solution-processed solar cells. *Adv. Mater.* **26,** 4741-4747 (2014).

(25) Pradhan, S., Stavrinadis, A., Gupta, S., Christodoulou, S. & Konstantatos, G. Breaking the open-circuit voltage deficit floor in pbs quantum dot solar cells through synergistic ligand and architecture engineering. *ACS Energy Lett.* **2,** 1444–1449 (2017).

(26) Carey, G. H., Levina, L. Comin, R., Voznyy, O. & Sargent, E. H. Record charge carrier diffusion length in colloidal quantum dot solids via mutual dot-to-dot surface passivation. *Adv. Mater.* **27,** 3325-3330 (2015).

(27) Zhitomirsky, D. *et al.* Engineering colloidal quantum dot solids within and beyond the mobility-invariant regime. *Nat. Commun.* **5,** 3803 (2014).

(28) Bi, Y. *et al.* Infrared solution-processed quantum dot solar cells reaching external quantum efficiency of 80% at 1.35 µm and J_{SC} in excess of 34 mA cm^{-2}. *Adv. Mater.* **30,** 1704928 (2018).

(29) Pradhan, S. *et al.* Trap-state suppression and improved charge transport in pbs quantum dot solar cells with synergistic mixed-ligand treatments. *Small* **13,** 1700598 (2017).

(30) Bi, Y. *et al.* Colloidal quantum dot tandem solar cells using chemical vapor deposited graphene as an atomically thin intermediate recombination layer. *ACS Energy Lett.* **3,** 1753–1759 (2018).

(31) Qian, L. *et al.* Electroluminescence from light-emitting polymer/ZnO nanoparticle heterojunctions at sub-bandgap voltages. *Nano Today* **5,** 384–389 (2010).

(32) Ji, W. *et al.* The work mechanism and sub-bandgap-voltage electroluminescence in inverted quantum dot light-emitting diodes. *Sci. Reports* **4,** 6974 (2014).

(33) Li, J. *et al.* Single-layer halide perovskite light-emitting diodes with sub-band gap turn-on voltage and high brightness. *J. Phys. Chem. Lett.* **7,** 4059−4066 (2016).

(34) Nagpal, P. & Klimov, V. I. Role of mid-gap states in charge transport and photoconductivity in semiconductor nanocrystal films. *Nat. Commun.* **2,** 486 (2011).

(35) Bae, W. K. *et al.* Controlling the influence of Auger recombination on the performance of quantum-dot light-emitting diodes. *Nat. Commun.* **4,** 2661 (2013).

(36) Cao, Y., Stavrinadis, A., Lasanta, T., So, D. & Konstantatos, G. The role of surface passivation for efficient and photostable PbS quantum dot solar cells. *Nat. Energy* **1,** 16035 (2016).

(37) Zhitomirsky, D.,Voznyy, O., Hoogland, S. & Sargent, E. H. Measuring charge carrier diffusion in coupled colloidal quantum dot solids. *ACS Nano* **7,** 5282–5290 (2013).

(38) Ushakova, E. V. *et al.* Anomalous size-dependent decay of low-energy luminescence from PbS quantum dots in colloidal solution. *ACS Nano* **6,** 8913–8921 (2012).

(39) Zhou, Y. *et al.* Near Infrared, Highly efficient luminescent solar concentrators. *Adv. Energy Mater.* **6,** 1501913 (2016).

(40) Rau, U. Reciprocity relation between photovoltaic quantum efficiency and electroluminescent emission of solar cells. *Phys. Rev. B* **76,** 085303 (2007).

(41) Yao, J. *et al.* Quantifying losses in open-circuit voltage in solution-processable solar cells. *Phys. Rev. Applied* **4,** 014020 (2015).

(42) Tress, W. Perovskite solar cells on the way to their radiative efficiency limit – insights into a success story of high open-circuit voltage and low recombination. *Adv. Energy Mater.* **7,** 1602358 (2017).

(43) Chuang, C. –H. M., Brown, P. R., Bulović, V. & Bawendi, M. G. Improved performance and stability in quantum dot solar cells through band alignment engineering. *Nat. Mater.* **13,** 796-801 (2014).

(44) Chuang, C. –H. M *et al.* Open-circuit voltage deficit, radiative sub-bandgap states, and prospects in quantum dot solar cells. *Nano Lett.* **15,** 3286– 3294 (2015).

(45) Walter, T., Herberholz, R., Müller, G. & Schock, H. W. Determination of defect distributions from admittance measurements and application to Cu(In,Ga)Se2 based heterojunctions. *J. Appl. Phys.* **80,** 4411 (1996).

(46) Bozyigit, D., Volk, S., Yarema, O. & Wood, V. Quantification of deep traps in nanocrystal solids, their electronic properties, and their influence on device behavior. *Nano Lett.* **13,** 5284–5288 (2013).

(47) Sun, B. *et al.* Multibandgap quantum dot ensembles for solar-matched infrared energy harvesting. *Nat. Commun.* **9,** 4003 (2018).

(48) Lee, J. W., Kim, D. Y., Baek, S., Yu, H. & So, F. Inorganic UV–Visible–SWIR broadband photodetector based on monodisperse PbS nanocrystals. *Small* **12,** 1328-1333 (2016).

(49) de Mello, J. C., Wittmann, H. F. & Friend, R. H. An improved experimental determination of external photoluminescence quantum efficiency. *Adv. Mater.* **9,** 230–232 (1997).
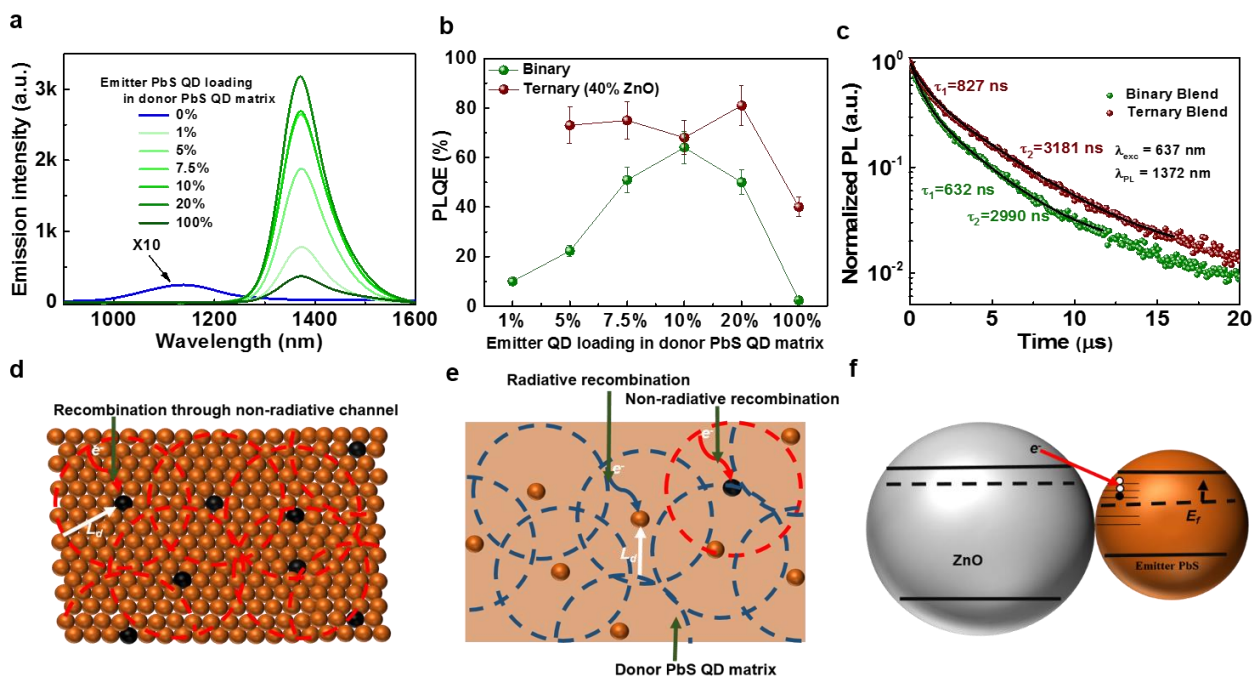
Figures
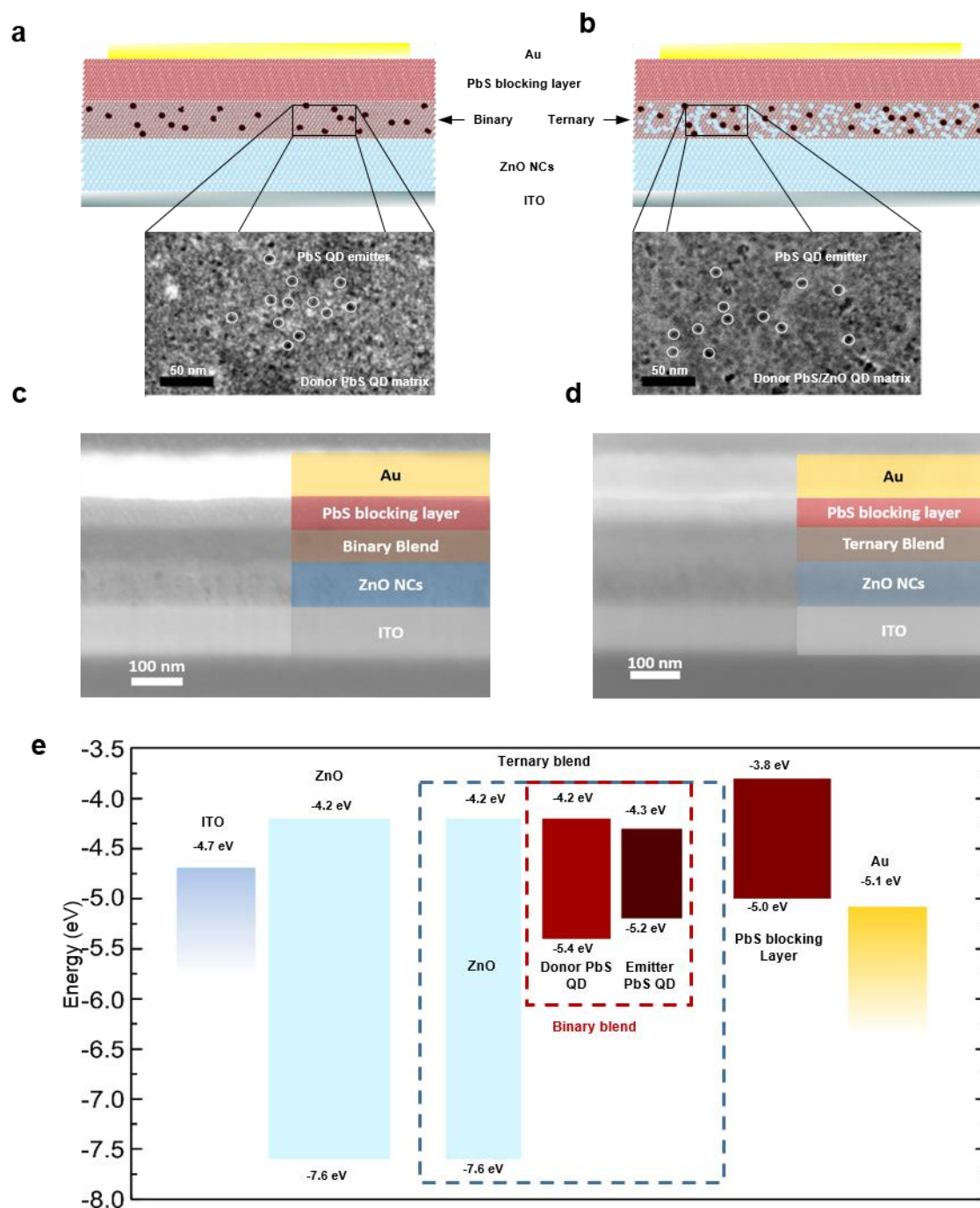
Figure 1: Device structure and composition of the binary and ternary blend based LEDs.
a,b. Schematic structure of LED devices with binary (**a**) and ternary (**b**) blend. TEM images of ligand treated binary and ternary blends respectively that comprise the active layer of the corresponding LEDs are shown as well. Circular white markers show the emitter QDs in donor matrix. **c,d.** FIB SEM cross-sectional images of binary(**c**) and ternary (**d**) blend based LED devices. **e**. Energy level diagram of the materials that constitute the LED devices. The energy values are taken from UPS measurements.
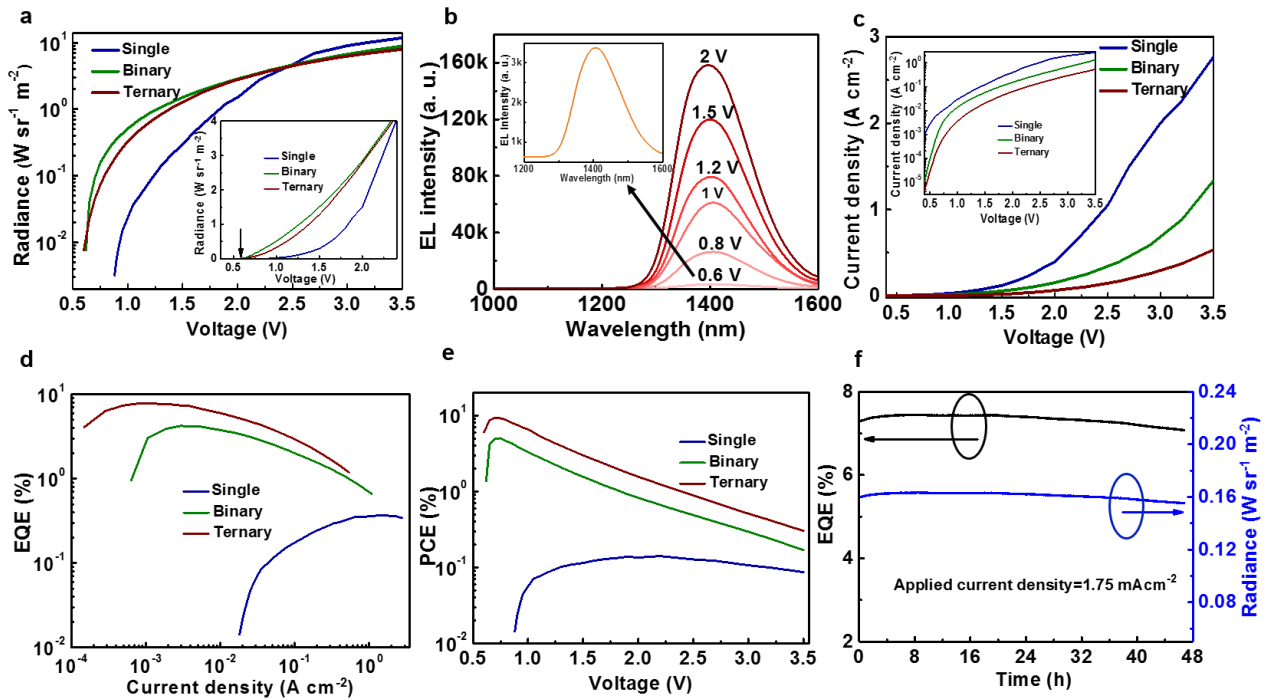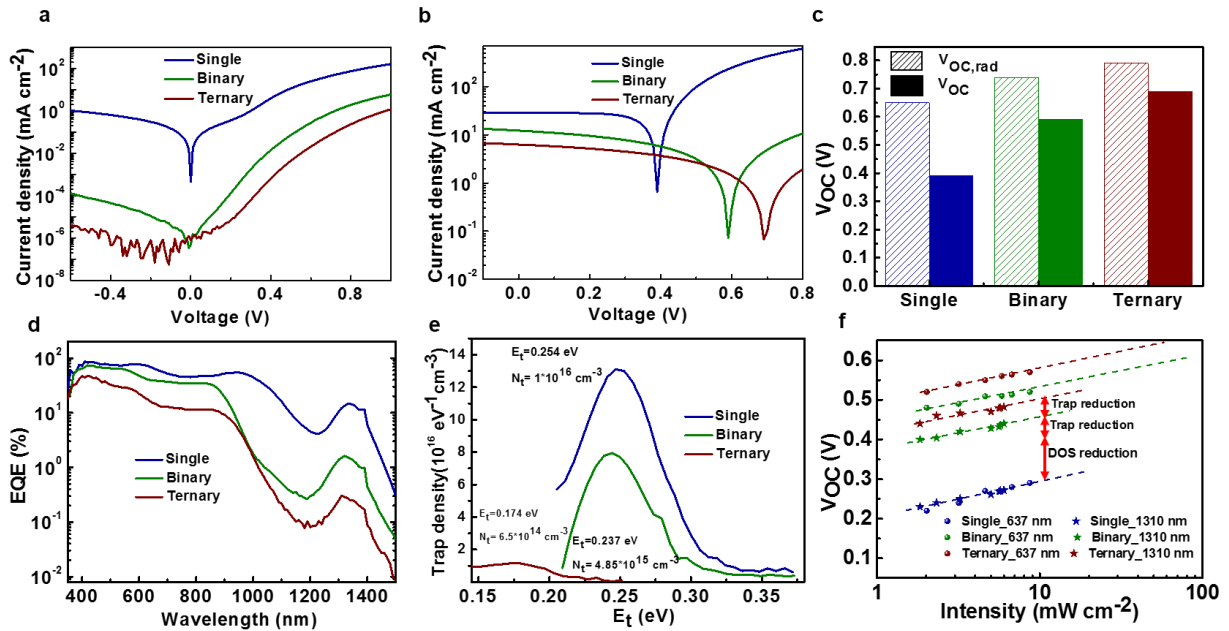
Figure 2: Performance of LED devices. a. Radiance of the devices with applied voltage bias. Inset shows the radiance in linear scale to indicate the turn-on voltage. The arrow shows the low turn-on voltage of 0.6 V in case of binary and ternary devices. **b.** EL spectra of ternary blend device with different applied bias voltage. Inset shows the zoomed EL spectra with 0.6 V applied bias. Strong sub-bandgap emission is observed in the devices. **c.** Injection current density is plotted as a function of applied bias. Inset shows the logarithmic plot to indicate the gradual suppression of leakage current from single to binary and further to ternary devices. **d**. EQE of the devices are plotted against injected current. **e.** PCE of the devices with applied voltage bias. **f.** Stability test of the champion device. The radiance and EQE of the device are observed with a constant applied current density of 1.75 mA cm^{-2} over a period of 48 hours.

Figure 3: PLQE and PL dynamics of QD blends. a. Evolution of PL spectra with different emitter QD loading in donor QD matrix. The loading of emitter QD completely quench the PL emission from the donor matrix and enhance the emitter QD band-edge PL intensity. **b.** PLQE of binary and ternary QD blends with different emitter QD loading in donor QD matrix. For ternary mixing, 40% ZnO NCs mixed with different binary blends. The error bars reflect the instrumental tolerance as described in the Methods. **c.** PL decay plots for binary and ternary blends upon pulsed excitation with 637 nm light. The curves are fitted with bi-exponential decays. The faster component is ascribed to the emitter QD PL life time whereas the slower component is attributed to the carrier supply lifetime of the photogenerated carriers in the matrix to the emitter QDs. **d,e.** Schematic diagram of charge recombination in emitter only QD arrays (**d**) and emitter QDs in donor QD matrix (**e**). The black spheres represents the defective QDs in arrays (as channels for non-radiative recombination). The charge collection zone of defective QDs determined by the carrier diffusion length (L_d) are shown as red circles around the QDs. (**e**) By loading emitter QDs in a donor QD matrix, the number of non-radiative recombination channels per volume decrease and radiative recombination channels increase through charge transfer from donor QDs to emitter QDs (blue circles). **f.** The schematic representation of remote trap passivation of PbS QDs through electron transfer from ZnO NCs. The empty traps (white circles) are filled by the electrons of the n-type ZnO NCs.

Figure 4: Photovoltaic performance, quantified trap-state analysis via TAS and V$_{OC}$ dependence of the single, binary and ternary QD blend devices. a,b. Dark and AM1.5 irradiated J-V plot of the three devices under study. Decrease of reverse saturation current is observed in accordance with the V$_{OC}$ evolution from single to ternary blend devices **(a).**The V$_{OC}$ of the devices increases from single to binary blend and further to ternary blend **(b). c.** Radiative V$_{OC}$ limit estimation by calculating luminescence EQE of PV. The solid columns indicate the V$_{OC}$ of the devices and lined columns indicate radiative V$_{OC}$. Decrease of non-radiative V$_{OC}$ losses observed from single to binary device and further to ternary device. **d.** EQE of PV devices based on single, binary and ternary QDs. **e.** Quantification of density of in-gap trap states from TAS analysis. Binary blend shows reduced traps with slight decrease of trap energy (E_t). Ternary blend shows significant decrease of traps as well as E_t as a result of trap passivation. **f.** Intensity dependent V$_{OC}$ variation of the devices under study with two different excitation wavelengths (637 nm and 1310 nm). 637 nm laser excites both emitter and matrix PbS QDs whereas 1310 nm light excites only the emitter QDs. The change of V$_{OC}$ from single to binary device is a combined effect of trap passivation and DOS reduction whereas the change from binary to ternary is mainly because of trap passivation.

Tables

Table 1: EQE values of LEDs varying the PbS QD matrix and the PbS QD emitter bandgaps

		Average EQE (%)
PbS QD matrix bandgap 1.49 eV / PbS QD emitter bandgap:	0.91 eV	6.7±0.4
	0.89 eV	7.11±0.30
	0.85 eV	4.95±0.40
PbS QD emitter bandgap 0.91 eV / PbS QD matrix bandgap:	1.24 eV	3.26±0.22
	1.31 eV	4.94±0.32
	1.49 eV	6.7±0.4

Table 2: Summary of the LED performance parameters for different devices.

Device	PLQE (%)	IQE (%)	$\eta_{carrier\ supply}$ (%)	EQE (%)
Single	2.3	~1.68	~73	0.4
Binary	51	~18.9	~37	4.5
Ternary	75.0	~33.2	~44	7.9